Title

Single cell-based fluorescence lifetime imaging of intracellular oxygenation and metabolism.

Authors

Penjweini, Rozhin

Roarke, Branden

Alspaugh, Greg

et al.

Publication Date

2020-07-01

DOI

10.1016/j.redox.2020.101549

Redox Biology 34 (2020) 101549

Contents lists available at ScienceDirect

Redox Biology

journal homepage: www.elsevier.com/locate/redox

Single cell-based fluorescence lifetime imaging of intracellular oxygenation and metabolism

Rozhin Penjweini[a], Branden Roarke[a], Greg Alspaugh[a], Anahit Gevorgyan[a], Alessio Andreoni[a,b], Alessandra Pasut[c], Dan L. Sackett[d], Jay R. Knutson[a,*]

[a] Laboratory of Advanced Microscopy and Biophotonics, National Heart, Lung, and Blood Institute (NHLBI), National Institutes of Health (NIH), Building 10, Room 5D14, Bethesda, MD, 20892-1412, USA
[b] Laboratory of Optical Neurophysiology, Department of Biochemistry and Molecular Medicine, University of California Davis, Tupper Hall, Davis, CA, 95616, USA
[c] Laboratory of Angiogenesis and Vascular Metabolism, Center for Cancer Biology, VIB, Leuven Cancer Institute, KU Leuven, Leuven, 3000, Belgium
[d] Cytoskeletal Dynamics Group, Division of Basic and Translational Biophysics, Eunice Kennedy Shriver National Institute of Child Health and Human Development (NICHD), National Institutes of Health (NIH), Building 9, Room 1E129, Bethesda, MD, 20892-0924, USA

ARTICLE INFO

Keywords:
Myo-mCherry
FLIM
Free and bound NAD(P)H
FAD
ORR
FLIRR

ABSTRACT

Oxidation-reduction chemistry is fundamental to the metabolism of all living organisms, and hence quantifying the principal redox players is important for a comprehensive understanding of cell metabolism in normal and pathological states. In mammalian cells, this is accomplished by measuring oxygen partial pressure (pO_2) in parallel with free and enzyme-bound reduced nicotinamide adenine dinucleotide (phosphate) [H] (NAD(P)H) and flavin adenine dinucleotide (FAD, a proxy for NAD^+). Previous optical methods for these measurements had accompanying problems of cytotoxicity, slow speed, population averaging, and inability to measure all redox parameters simultaneously. Herein we present a Förster resonance energy transfer (FRET)-based oxygen sensor, Myoglobin-mCherry, compatible with fluorescence lifetime imaging (FLIM)-based measurement of nicotinamide coenzyme state. This offers a contemporaneous reading of metabolic activity through real-time, non-invasive, cell-by-cell intracellular pO_2 and coenzyme status monitoring in living cells. Additionally, this method reveals intracellular spatial heterogeneity and cell-to-cell variation in oxygenation and coenzyme states.

1. Introduction

Nicotinamide adenine dinucleotide (NAD^+) and oxidized flavin adenine dinucleotide (FAD) are the two major cofactors in cellular redox reactions and central regulators of energy production and metabolism [1,2]. Reduced nicotinamide adenine dinucleotide (phosphate) [H] (NAD(P)H) exists in a free and a protein-bound functional form, and it serves as a coenzyme and principal electron donor within the cell for oxidative phosphorylation (OXPHOS, aerobic respiration) and glycolysis (anaerobic respiration) [3]. Bound NAD(P)H is associated mostly with the dehydrogenases of respiratory complex I, one of the four mitochondrial membrane protein complexes that mediate electron transfer from NAD(P)H to molecular oxygen (O_2) and use the energy derived from this reduction reaction to pump protons from the mitochondrial matrix into the intermembrane space. This gradient of protons and electrical potential is subsequently utilized by the adenosine triphosphate (ATP) synthase enzyme complex to synthesize new ATP molecules via adenosine diphosphate (ADP) phosphorylation [4]. Enzyme-bound forms of NAD(P)H are likely associated with energy generation in the form of ATP, and the relative quantities of free and bound species provide an insight to the metabolic state of a cell [5]. Moreover, it is known that the reaction velocity of a given intracellular NAD(P)H-linked dehydrogenase depends on the local concentration of free NAD(P)H [3].

FAD, like NAD(P)H, is also a key cofactor in cellular energetics. Inside mitochondria, one molecule of FAD is reduced to $FADH_2$ in the tricarboxylic acid cycle (TCA), and $FADH_2$ is oxidized back to FAD by respiratory complex II of the electron transport chain (ETC) [6,7]. Acyl-CoA dehydrogenases, electron transferring flavoprotein (ETF), and ETF dehydrogenase are key mitochondrial FAD containing enzymes that work together in lipid and branched-chain amino acid catabolism to ultimately shuttle electrons from these energy sources to complex III of the ETC [8,9]. Many other cellular regulatory processes, such as reactive oxygen species (ROS) production, antioxidant defense, protein folding, peroxisome functioning, and chromatin remodeling (which is crucial for cell life and death), are also dependent on more than 100

* Corresponding author.
E-mail address: knutsonj@nhlbi.nih.gov (J.R. Knutson).

https://doi.org/10.1016/j.redox.2020.101549
Received 27 February 2020; Received in revised form 15 April 2020; Accepted 20 April 2020
Available online 27 April 2020

different flavoproteins, of which 75% use FAD as a cofactor [6]. A schematic overview of the respiratory chain, as well as NAD(P)H and FAD oxidation and reduction sites can be found in Supplemental Fig. S1.

The metabolic cofactors NAD(P)H and FAD are endogenously fluorescent in one of their redox forms while dark in the other: NAD(P)H and FAD are the fluorescent species, whereas NAD^+ and $FADH_2$ are non-emitting. Furthermore, their different spectral excitation and emission features allow for separate detection when using the appropriate combination of laser lines and filter sets [10–12]. Thanks to these properties, it is possible to measure the so-called optical redox ratio (ORR), defined as the intensity ratio of FAD/(NAD(P)H + FAD), and the fluorescence lifetime redox ratio (FLIRR), defined as the ratio of bound NAD(P)H/bound FAD [10,13–15]. ORR and FLIRR dynamically change upon imbalances of O_2 consumption and supply in response to the microenvironment, cellular activity and/or in the course of many (patho)physiological conditions, including ischemia/stroke, excitotoxicity, neurodegeneration, cancer, and inflammation [16,17]. ORR is proportional to the more traditional oxidation-reduction ratio of NAD^+/NAD(P)H [18]: higher ORR values indicate that cells are more oxidative, whereas lower ORR values reflect greater glycolytic metabolism [19]. Increased metabolic activity is also measured through increased FLIRR, providing equivalent information as ORR, however, FLIM measurements have the advantage of being largely unaffected by intensity-based limitations [14,20].

Considerable research has been devoted to detecting the intrinsic fluorescence of NAD(P)H and FAD, which primarily are found within mitochondria, by using two-photon, near infrared (NIR) excitation [18,19,21]. This excitation method has revealed that the fluorescence lifetimes of NAD(P)H and FAD change upon binding to proteins within the electron transport chain [3,22]; thus, fluorescence lifetime imaging (FLIM) has been used to provide sensitive measurements of the free and protein-bound NAD(P)H and FAD ratio to estimate the contribution of OXPHOS versus glycolysis in ATP production [1,2], as well as the overall redox state of cells [18,23]. In contrast, the cellular metabolic responses to alterations in O_2 supply or demand have not yet been rigorously evaluated, partly because O_2-sensing techniques are often incompatible with measurements of NAD(P)H and FAD concentrations. Furthermore, many O_2-sensing techniques are invasive, low resolution, limited to recording mitochondria, disrupt normal cellular functions or are unable to reveal heterogeneity at the subcellular level [24,25]. Moreover, the general view of mitochondrial and cellular oxygenation and metabolism is biased by the high oxygen partial pressure range used in most *in vitro* measurements (air saturated pO_2 ~150 mmHg). While physiological pO_2 level below 40 mmHg [26,27] and mitochondrial pO_2 level below 7.5 mmHg [28] are understood to significantly impact the phenotype of cells in the abstract, in practice the importance of the imposed pO_2 does not appear to be well recognized in the non-specialist research community [29,30].

Our previous work introduced Myoglobin-mCherry (Myo-mCherry) as a novel, genetically encoded Förster resonance energy transfer (FRET)-based O_2-sensor able to map intracellular pO_2 [24]. The working principle of the sensor relies on FRET between the fluorescent protein mCherry and the dark acceptor myoglobin, whose spectral features change upon O_2 binding, thus modulating the energy transfer as a function of O_2 concentration. To prevent artefacts generally associated with intensity-based FRET [31], we used fluorescence lifetime measurements instead, to measure changes in energy transfer. In this study, we use two-photon FLIM to simultaneously measure intracellular NAD(P)H, FAD, and pO_2 in cultured cells with minimal cytotoxicity and excellent spatial resolution by exploiting the autofluorescence of NAD(P)H and FAD, as well as the features of the Myo-mCherry probe. We demonstrate how changes in the media-imposed pO_2 (from 1 to 140 mmHg) influence (i) heterogeneous intracellular pO_2 distributions (ii) the normalized ratio of free- and bound-NAD(P)H and FAD, and (iii) ORR and FLIRR in three human cancer cell lines: A549 (lung), HeLa (cervical), and HepG2 (liver). These cell lines are known to differ in O_2 consumption rates and metabolism [32,33], and are broadly used as cell models. For these reasons, we believe that our unprecedented insight into cellular metabolic responses to intracellular O_2 variations will benefit the cancer community that routinely uses cancer cell lines in their studies.

2. Materials and methods

2.1. Myo-mCherry plasmid preparation

The plasmid coding for Myo-mCherry was prepared as described previously [24,34]. Briefly, the pmCherry N1 vector (Clonetech, Mountain View, CA, USA) was used as a template to introduce the myoglobin gene (*Physeter catodon*, Sperm Whale, Addgene Plasmid pMB413a, #20058) at the N-terminus of the fluorescent protein. A 2-residue glycine-serine linker was inserted in between the two proteins to allow for flexibility and prevent misfolding [35]. Gene insertion was performed either with a Gibson assembly method (New England BioLabs, Ipswich, MA, USA), or In-Fusion molecular cloning (Takara Bio, Mountain View, CA, USA). Expression in eukaryotic cells is obtained via the CMV promoter and enhancer originally present in the pmCherry N1 used as a template. Sequences of the final products were verified via Sanger sequencing.

2.2. Transfection of eukaryotic cells

A549, HeLa, and HepG2 Cells were kept in Dulbecco's modified Eagle's medium (DMEM, Gibco, Grand Island, NY, USA) combined with 10% fetal bovine serum, and 1% penicillin-streptomycin solution (Mediatech Inc. Manassas, VA, USA). The cells were plated in a μ-Slide 4 well chamber (Ibidi GmbH, Martinsried, Germany) with a density of 10^4 cells/cm^2. Cells were then transfected using Lipofectamine® 2000 DNA transfection reagent (Invitrogen, Carlsbad, CA, USA). 3.5 μL of DNA solution was diluted in a 72:1 ratio with Opti-MEM® medium (Gibco). The diluted DNA solution was then combined one to one with a 10:1 dilution of Opti-MEM® to Lipofectamine® 2000. After a 20-min incubation period, the DNA-Lipofectamine transfection complex was added to each chamber, along with 400 μL of DMEM. The cells were then allowed to incubate at 37 °C and 5% CO_2 with a final plasmid amount of ~10 ng per well. After 48 h the transfection media was removed, and the cells were washed with phosphate buffered saline (PBS, Gibco). The cells were then covered with 400 μL of fresh DMEM for imaging.

2.3. Treatment of the cells with rotenone and antimycin A or 2,4-Dinitrophenol (DNP)

Different concentrations of 2,4-Dinitrophenol (DNP; Sigma-Aldrich, St Louis, MO, USA) and combinations of rotenone/antimycin (Sigma-Aldrich) with varying incubation times were explored to develop a protocol that allows for prolonged imaging while preventing cell death in the presence of these drugs. DNP transports protons across the mitochondrial inner membrane, altering the proton gradient and inhibiting ATP production via OXPHOS. An increase in proton conductance leads to an increase in the respiratory rate and O_2 consumption. Rotenone inhibits the transfer of electrons from complex I to co-enzyme Q (CoQ), whereas antimycin prevents the oxidation of CoQ by cytochrome c. The rotenone/antimycin combination allows for inhibition of respiration and mitochondrial O_2 consumption. The changes of intracellular pO_2 and its effects on metabolism upon increase or decrease of O_2 consumption were monitored with 50 μM DNP or a mixture of 2 μM rotenone/antimycin, respectively. Using these concentrations, it was possible to monitor the increase or decrease of O_2 consumption for at least 4 h. It is worth noting that the interaction of cyanide (CN^-), found in more commonly used uncouplers such as

carbonyl cyanide-4-(trifluoromethoxy)phenylhydrazone (FCCP) and carbonyl cyanide m-chlorophenyl hydrazone (CCCP), with the heme in Myo-mCherry could alter FRET, interfere with the lifetime measurements and cause misinterpretation of the corresponding pO_2 levels.

2.4. Imaging setup

Two photon FLIM was performed using a Leica SP5 confocal laser scanning microscope (Buffalo Grove, IL) equipped with a tunable Chameleon Ti:Sapphire femtosecond laser (Coherent, UK) operating at 80 MHz with wavelengths set to 720, 780, and 850 nm for the excitation of NAD(P)H, Myo-mCherry, and FAD respectively. The two-photon action cross-section of NAD(P)H decreases by several orders of magnitude between 720 nm and 850 nm excitation, enabling an efficient isolation of FAD at longer wavelengths [1]. The excitation light was passed through a 685 nm LP dichroic mirror and directed to the back aperture of a Leica Plan-Apochromat 40 × , 1.1 NA water immersion microscope objective. The laser power at the back aperture of the objective was kept below 7 mW to avoid photobleaching during the extended collection time required for FLIM. The emission was collected through the same objective, directed to the side port of the microscope (non-descanned detection) and passed through a 680 nm short pass filter (Leica) to reduce scattering from the laser. A 560 nm long pass dichroic mirror was used to split the emission from NAD(P)H and FAD toward two different detectors. The signal from NAD(P)H was further filtered through a 460/60 nm bandpass, whereas a 552/57 nm bandpass was used for FAD (Semrock BrightLine®, Rochester, NY, USA). The signal from mCherry was filtered through a 647/57 nm bandpass filter (Semrock BrightLine®, Rochester, NY, USA). The filtered signals were focused on two hybrid photomultiplier detectors (HyD, Leica Microsystems) with high sensitivity and timing accuracy. The photomultiplier tube (PMT) gain was adjusted for each image to maximize contrast while preventing signal saturation at individual pixels. The electrical pulse output from the HyD was directed into an SPC-150 photon counting card (Becker & Hickl, Berlin, Germany). The signals were synchronized with the pulses from the laser to allow for time-correlated single photon counting (TCSPC). Synchronization with the pixel, line, and frame clock from the scanning unit of the microscope was used for image construction in TCSPC mode. Single cells were imaged for 50–80 s (depending on the intensity) to accumulate an adequate number of photons per pixel for further analysis. Image size was set to 256 × 256 $(pixels)^2$, and TCSPC histograms were collected with 256 channels in a 12.5 ns time window (~48 ps per channel). Due to the different requirements in excitation and emission settings for each cell, the signal from NAD(P)H, FAD and Myo-mCherry were recorded sequentially in this order with only a few seconds delay between the end of one measurement and the beginning of the next one.

2.5. Controlled external pO_2 during imaging

A miniature incubation chamber (Bioscience Tools, San Diego, CA, USA) was mounted onto the microscope stage and connected to a gas mixing system (CO_2–O_2 − MI, Bioscience Tools, San Diego, CA, USA) to provide and maintain a suitable environment for cells during imaging. The incubator kept the temperature at 37 °C, and the gas mixing system delivered mixtures of N_2, O_2, and CO_2 inside the chamber according to the inputs set by the user. FLIM recordings were performed at stable % O_2 (v/v) of 20%, 16%, 13%, 10%, 7%, 4%, 1% and 0.5% in the microscope chamber, where 0.5% is the lowest $\%O_2$ attainable by our system. Typically, the cell culture (in culture dishes with a ~ 3 mm layer of medium above cells, without lids), when monitored by a 250 μm diameter bare-fiber O_2 sensor (NX-BF/O/E, Optronix Ltd., Oxford, UK) connected to an OxyLite, 1 Channel monitor (Optronix Ltd., Oxford, UK), reaches a stable pO_2 within 45 min. The media-imposed external pO_2 (in mmHg) was measured at the bottom of the 4-well chamber with or without live cells present.

2.6. Fluorescence lifetime analyses

Fluorescence lifetime decay images of samples at each external pO_2 were analyzed using the software SPCImage (Becker & Hickl GmbH, Berlin, Germany). As we described previously [24], the decay curves at each pixel were fit using a non-linear least-squares method to follow a double-exponential decay model:

$$F(t) = a_1\, exp\,(t / \tau_1) + a_2\, exp\,(t / \tau_2) \quad (1)$$

where a_1 and a_2 are pre-exponential factors and can be used (if natural lifetime is constant) to represent the fraction of fluorophores with shorter (τ_1) and longer (τ_2) lifetimes, respectively.

The instrument response function (IRF) was measured using second harmonic signals generated within and scattering from small urea crystals. IRF was used during the analysis process through iterative reconvolution with the decay model to account for the convolved temporal width of the laser pulses and the detector response function. The color-shift of the IRF was determined by fitting the decay of the pixel with the highest intensity in each image, allowing the color-shift parameter to run free, and it was then fixed for the fitting of the entire FLIM image. The lifetime decays of mCherry (in the presence or absence of the FRET acceptor myoglobin), NAD(P)H and FAD were obtained by a multiexponential model in SPCImage at optimized goodness of fit (χ^2) [20,24]. The intracellular distribution of Myo-mCherry, NAD(P)H and FAD is heterogeneous, which results in variable fluorescence intensity across different cells. To avoid fitting decays with a peak count lower than 1000, binning of adjacent pixels (setting: 5–7 in SPCImage) was used. Although high optical density two-photon filters were employed to remove scattered laser light before the detectors, we cannot exclude bleed-through that might occur due to scattering within the cell, caused by slight variations in refractive index, intracellular composition, and organelle arrangement. Therefore, a scatter parameter was included in the fitting model. A number of parameters including τ_1, τ_2, a_1%, a_2%, normalized a_1 and a_2 ($|a_1|$ and $|a_2|$), average lifetime (τ_{mean}), and χ^2 were generated via amplitude weighting for each pixel. Finally, color-mapped lifetime images of Myo-mCherry and the corresponding free/bound distribution of NAD(P)H ($a_1\%/a_2\%$) in the intracellular environment were obtained for each cell.

2.7. Calculation and mapping of the intracellular pO_2

The fluorescence lifetime at each set value of pO_2, $\tau(pO_2)$, was calculated by taking the mean lifetime from each single image and averaging this across multiple cells (n > 30). The resulting lifetime values were plotted against the media-imposed external pO_2, and a hyperbolic curve was fit to the data using the Curve Fitting Toolbox in MATLAB R2016b (The MathWorks Inc., Natick, Massachusetts):

$$\tau(pO_2) = (\tau_{max} - 0.914)\frac{pO_2}{K + pO_2} + 0.914 \quad (2)$$

where 0.914 ns is the shortest average lifetime obtained for Myo-mCherry at hypoxia. τ_{max} is the longest average lifetime for Myo-mCherry at normoxia for each dataset, and we found this to vary with cell type. K is a fitting parameter related to the affinity of myoglobin for O_2.

This hyperbolic equation was thought reasonable since the probe seems to follow the O_2 dissociation behavior of myoglobin as described in our previous publication [24]. To obtain intracellular pO_2, $\tau(pO_2)$ in A549, HeLa, and HepG2 cells were compared to those measured in cells treated with rotenone/antimycin. Since cells treated with rotenone/antimycin are incapable of significant O_2 consumption, intracellular pO_2 is assumed in this case to be equivalent to the media-imposed pO_2. Therefore, the $\tau(pO_2)$ values of the treated cells can be used as a reference for the lifetime of the probe at the environmental level of pO_2 present in solution. Rearranging Eq. (2), it is possible to back calculate

Table 1
Parameters of the hyperbolic fits. Fitting parameter K was obtained from fitting the data presented in Fig. 1A–Eq. (2). τ_{max} is the longest average lifetime for Myo-mCherry in each cell type measured at normoxia (O_2 = 20%). Each parameter is shown with its standard deviation.

	τ_{max} (ns)	K (mmHg)	R^2
DNP	1.19 ± 0.03	8.395 ± 3.622	0.94
A549	1.22 ± 0.03	9.063 ± 2.588	0.98
HeLa	1.26 ± 0.04	6.057 ± 1.520	0.99
HepG2	1.28 ± 0.04	3.139 ± 0.976	0.98
Rotenone/Antimycin	1.30 ± 0.04	2.786 ± 0.606	0.99

the effective pO_2 at each lifetime value, fixing the K and τ_{max} to the values obtained from the rotenone/antimycin data. In agreement with a previous study of a related system [36,37], we found a hyperbolic relationship between the pO_2 in the media surrounding the cells and the measured intracellular pO_2 ($pO_{2\ intra}$).

Intracellular pseudocolor mapping of $pO_{2\ intra}$ in A549, HeLa, and HepG2 cells was obtained using MATLAB R2019b (The MathWorks Inc.) equipped with the Image Processing Toolbox. Analyzed lifetime image parameters (a_1, a_2, τ_1, τ_2) at each pixel were exported from SPCImage as ASCII files; additionally, a color image of the cell with an applied threshold and appropriate region of interest was exported to serve as a pixel mask and transparency map. Following application of the mask and calculation of the amplitude-weighted lifetime of Myo-mCherry at each pixel, the apparent $pO_{2\ intra}$ values were back-calculated using a modified binary search algorithm that mapped lifetimes to their appropriate values along the rotenone/antimycin calibration curve (see the fitting parameters in Table 1). Since we assume any $\tau(pO_2)$ values above τ_{max} for rotenone/antimycin treated cells (1.30 ns) are a consequence of photon counting noise in the (statistically weak) individual pixels, pixel pO_2 colormaps were truncated to the range of 0–140.1 mmHg, which is the highest pO_2 applied across experiments. Following back-calculations, the pO_2 maps were denoised with a median filter and were interpolated for presentation.

2.8. Calculation and intracellular mapping of ORR and FLIRR

At each imposed pO_2, ORR was calculated by using the intensity ratio of FAD/(NAD(P)H + FAD). NAD(P)H and FAD fluorescence were normalized to account for the PMT gain and laser power recorded for every image. We additionally calculated FLIRR, the FLIM-based redox ratio of bound NAD(P)H/bound FAD ($a_{2,NAD(P)H}$ %/$a_{1,FAD}$ %) to avoid potential intensity-related artefacts, such as photo-bleaching, light-scattering or fluctuations of illumination level [10]. The values of ORR and FLIRR were plotted against the intracellular pO_2 as measured through Myo-mCherry FLIM. Intracellular pseudocolor mapping of ORR and FLIRR in A549, HeLa, and HepG2 cells was conducted using MATLAB R2019b (The MathWorks Inc.) equipped with the Image Processing Toolbox. Briefly, analyzed lifetime image parameters (a_1, a_2, τ_1, τ_2, intensity) were exported from SPCImage; additionally, a color image of the cell was exported to serve as a pixel mask upon import into MATLAB. Following application of the mask and thresholding pixels with no amplitude signal, the ORR and FLIRR was calculated at each unmasked pixel and was assigned to a color and a transparency weight.

2.9. Statistical analyses

For each condition, FLIM was conducted for at least 30 cells. Kruskal-Wallis and Mann–Whitney U tests were used to evaluate whether the values in the independent groups are significantly different from each other. Analyses were carried out using SPSS 14.0 (a subsidiary of IBM, Chicago, IL, USA) software and statistical significance was defined at $p < 0.05$ (95% confidence level).

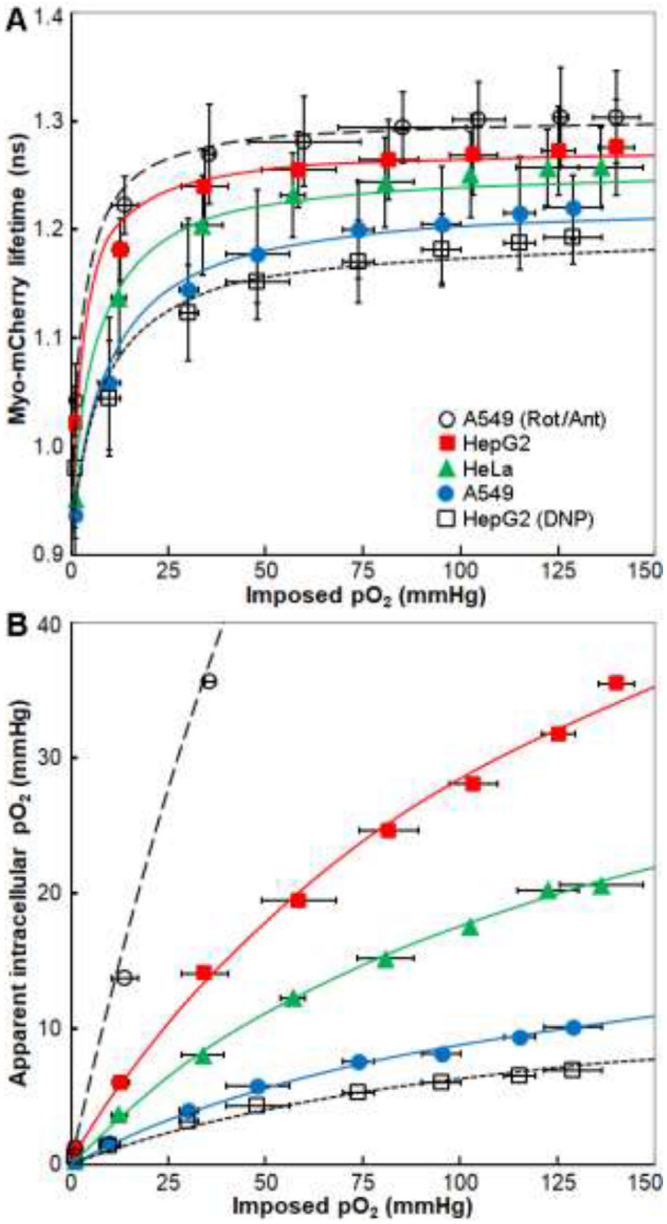

Fig. 1. Intracellular pO_2 obtained from Myo-mCherry lifetime. A) Average fluorescence lifetime of Myo-mCherry plotted versus the media-imposed pO_2, in A549 (blue-filled circle), HeLa (green-filled triangle), HepG2 (red-filled square), HepG2 treated with DNP (empty square), and A549 cells treated with rotenone/antimycin (empty circle). Cells were exposed to external O_2% from 20 to 0.5%; x axis reports the pO_2 in the media measured by OxyLite fiber proximate to the cell monolayer in three independent experiments. The data are shown with the best hyperbolic fit obtained from Eq. (2). B) The apparent intracellular pO_2 is plotted versus the applied media pO_2. The values of intracellular pO_2 were calculated from the FLIM data by using the calibration curve obtained from the cells treated with rotenone/antimycin. Vertical and horizontal error bars are the standard deviations. (For interpretation of the references to color in this figure legend, the reader is referred to the Web version of this article.)

3. Results and discussions

3.1. Measurement of the intracellular pO_2 using lifetime imaging of Myo-mCherry

The lifetime of Myo-mCherry as a function of pO_2 follows the hyperbolic O_2 dissociation behavior of myoglobin [24]. When the probe is deoxygenated, its emission intensity and (correspondingly) its lifetime

will decrease compared to its oxygenated form. As shown in Fig. 1A, the changes of Myo-mCherry lifetime in response to different imposed pO_2 (from 140 to 1 mmHg) were measured in A549 (blue-filled circle), HeLa (green-filled triangle), and HepG2 (red-filled square) cells. All three cell types were plated at the same density (10^4 cells/cm^2) and imaged under identical conditions. The best hyperbolic fit to the data was obtained using Eq. (2), and the obtained values of τ_{max}, the fitting parameter K, and the goodness of fit R^2 are shown in Table 1. Cells transfected with Myo-mCherry did not show any sign of cytotoxicity up to three days after transfection. The measurements for cytotoxicity and transfection efficiency of Myo-mCherry are shown in Supplemental Fig. S2.

The O_2 consumption of the cell monolayer at the bottom of the dish is a major determinant of O_2 diffusion since consumption determines the steepness of the O_2 concentration gradient in the media covering the cells. This effect will ultimately influence the pericellular pO_2 and as a consequence, low consuming cells are likely to experience greater intracellular pO_2 than those more rapidly consuming O_2 when placed in the same environment [38]. This phenomenon was confirmed by using an OxyLite probe to measure pO_2 close to the cell monolayer. Based on the results shown in Refs. [32], HepG2 cells have a lower O_2 consumption rate compared to HeLa and A549 cells. Accordingly, HepG2 cells transfected with Myo-mCherry yielded longer average lifetimes at all imposed pO_2 levels than the other cell types, which indicates a higher intracellular pO_2 than the other cell types. A549 cells, in contrast, have the highest O_2 consumption rate as compared to HepG2 and HeLa cells [32] and yielded shorter average lifetimes at all imposed pO_2 levels, and therefore lower intracellular pO_2. We further explored the effect of changing the cellular O_2 consumption on Myo-mCherry lifetime by adding the mitochondrial uncoupler DNP to HepG2 cells. As shown in Fig. 1A, the average lifetime in cells treated with DNP (empty squares) is consistently shorter when compared to untreated cells at the same imposed pO_2. The lifetime of Myo-mCherry in DNP treated cells decreased by 6.5% (from 1.28 ± 0.04 ns to 1.19 ± 0.03 ns) at the highest imposed pO_2 and 4.1% (from 1.02 ± 0.03 ns to 0.98 ± 0.05 ns) at the lowest imposed pO_2 when compared to the untreated HepG2 cells. The lifetime values in DNP treated cells were also shorter than those in HeLa and A549 cells at the same imposed pO_2, except at 1 mmHg.

The calibration of the Myo-mCherry sensor *in situ* for a specific cell line is performed by turning off all mitochondrial O_2 consumption by using rotenone/antimycin inhibitors to disrupt OXPHOS; non-mitochondrial O_2 consumption was assumed to be negligible due to its small contribution of 5–10% (see Supplemental section 3 for further illustration). All cell types treated with rotenone/antimycin showed similar average lifetime values at all media-imposed pO_2 (see Supplemental Fig. S3). Therefore, only the results for A549 cells are shown in Fig. 1A. As shown in Fig. 1A, the average lifetime in A549, HeLa, and HepG2 cells that are consuming O_2 consistently evince lower apparent pO_2 than the common rotenone/antimycin calibration curve. The lifetime of oxygenated Myo-mCherry in A549 cells treated with rotenone/antimycin (empty circle) increased by 6.4% (from 1.22 ± 0.03 ns to 1.30 ± 0.04 ns) at the highest imposed pO_2 and the lifetime of deoxygenated Myo-mCherry increased by 19.1% (from 0.94 ± 0.05 ns to 1.04 ± 0.03 ns) at the lowest pO_2. Mapping via the rotenone/antimycin fit curve formula in Eq. (2) (fitting parameters available in Table 1) allows one to transform and replot Fig. 1A as intracellular versus media-imposed pO_2 as seen in Fig. 1B. By examining a variety of anoxic through normoxic conditions, one can see that the intracellular versus imposed pO_2 trends are similar and hyperbolic for all cell types. Clearly, the sustained internal pO_2 levels that are well below those applied reveal differences in the O_2 consumption in A549, HeLa, and HepG2 cells. Based on the results, A549 cells reduced the pO_2 = 128.9 mmHg in covering media down to pO_2 = 10.19 mmHg inside the cells. HepG2 cells, in contrast, had the highest intracellular pO_2 as compared to the other cell types; the media-imposed pO_2 of 140 mmHg was reduced to 35.65 mmHg inside the cells. Kruskal-Wallis tests showed a statistically significant difference between the Myo-mCherry lifetimes and pO_2 values in the intracellular environment of A549, HeLa, and HepG2 cells. We do not yet quantify the gradient steepness between the media and intracellular compartment; that will require an external plasma membrane version of our probe (in development).

The differences between lifetime-detected intracellular pO_2 in these three cell types most likely arise from differences in mitochondrial O_2 consumption and activity [28,32,38]. In support of this, the average lifetime in HepG2 cells treated with mitochondrial uncoupler DNP (empty square in Fig. 1B), consuming O_2 at their highest possible rate, consistently evince lower intracellular pO_2 than the untreated cells (except for the convergence of all at the endpoint at imposed pO_2 ~ 1 mmHg). Note that we did not assume the media-imposed pO_2 is identical to that found at the cell surface in order to recover the apparent internal pO_2; that is only strictly needed for the reference curve with rotenone/antimycin. We leave to future studies the question of whether most of the media-imposed to intracellular gradient occurs inside or outside the membrane. The myoglobin-saturation controlled lifetime values still represent *in situ* metabolic pO_2.

We next sought explanation for the cell-type differences in pO_2. In an initial attempt to evaluate mitochondrial activity, western blots of each cell line were probed with antibodies for each of the mitochondrial ETC complexes. Unsurprisingly (given the complex regulation of metabolism by substrate and product feedback mechanisms), there was an inconclusive relationship between ETC protein amount and oxygenation. Further information regarding the blots can be found in Supplemental Fig. S4.

3.2. Imaging of the changes of free and bound NAD(P)H and FAD in response to intracellular pO_2

When the amount of O_2 is limited, OXPHOS capacity is reduced and glycolysis is enhanced in various cancer cells [15]. This causes resistance to fluctuations in the local O_2 and alterations in the tumor microenvironment that support tumor cell migration and invasion [10]. To monitor the activity of OXPHOS and glycolytic metabolism in A549, HeLa and HepG2 cells, lifetime imaging of the metabolic co-factors NAD(P)H and FAD was performed at different imposed pO_2 (from 140 to 1.0 mmHg). Then, their free and bound populations were correlated to the corresponding apparent intracellular pO_2 acquired from Myo-mCherry FLIM data shown in Fig. 1B. Based on our results, free NAD(P)H exhibited a fluorescence decay with a short lifetime (τ_1) of ~0.54 ± 0.04 ns and bound NAD(P)H had a longer lifetime (τ_2) of ~3.70 ± 0.06 ns in A549, HeLa and HepG2 cells. These values are in agreement with the wide spectrum of NAD(P)H FLIM studies currently published [39–42]. Free FAD exhibited a fluorescence decay with a long lifetime of ~2.23 ± 0.03 ns, and a shorter lifetime value of ~0.35 ± 0.04 ns was obtained for the bound form of FAD [12]. The percentage change in the free/bound NAD(P)H ratio (a_1%/a_2%), free/bound FAD ratio (a_2%/a_1%), and the normalized free and bound populations ($|a_1|$ and $|a_2|$) in response to the intracellular pO_2 are shown in Fig. 2A–F.

During OXPHOS (at higher pO_2) when NAD(P)H gets converted to NAD^+ by the enzyme NAD(P)H dehydrogenase [15], NAD(P)H exists predominantly in an enzyme bound state (lower a_1%/a_2%), whereas $FADH_2$ gets converted to non-enzyme bound FAD by the enzyme succinate dehydrogenase (lower bound FAD fraction, thus higher a_2%/a_1%) [10]. Accordingly, our FLIM results shown in Fig. 2A indicate lower NAD(P)H a_1%/a_2% at higher pO_2 and a 16–20% increase of the ratio upon hypoxia. In contrast to NAD(P)H, FAD was present largely in a free state at higher pO_2 and FAD a_2%/a_1% decreased by 6–7% upon hypoxia (Fig. 2B). We also identified differences between the normalized free and bound FAD as well as free NAD(P)H with no significant difference in bound NAD(P)H among A549, HeLa, and HepG2 cells (Fig. 2C–F). A lower free NAD(P)H ($|a_1|$) and higher free FAD ($|a_2|$) and

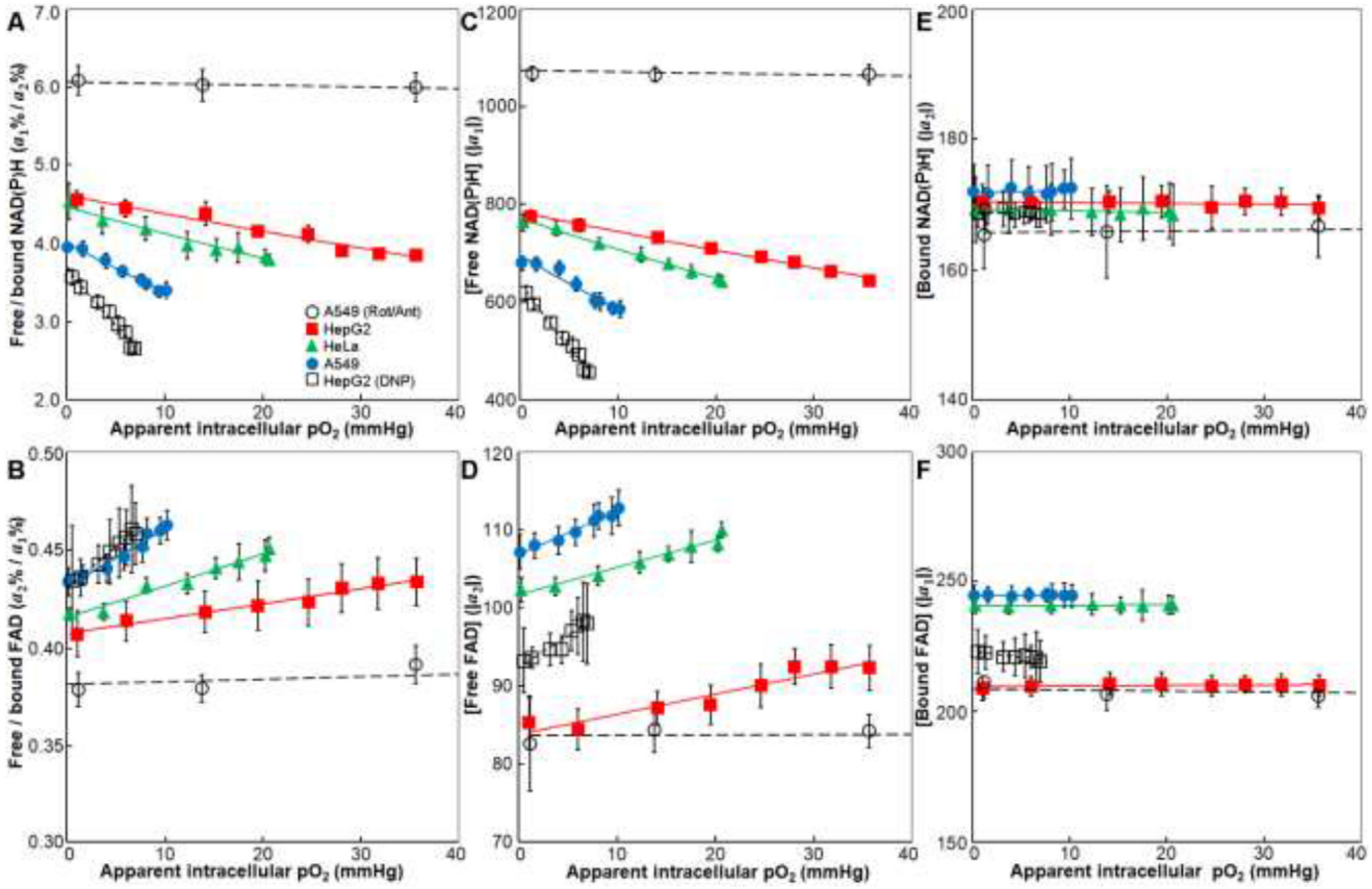

Fig. 2. Changes of free and enzyme-bound NADH and FAD versus apparent intracellular pO_2. A-B) The changes of free/bound NAD(P)H ratio (a_1%/a_2%), and free/bound FAD ratio (a_2%/a_1%) versus apparent intracellular pO_2. C-D) The changes of normalized free NAD(P)H ($|a_1|$) and FAD ($|a_2|$) versus the intracellular pO_2. E-F) The changes of normalized bound NAD(P)H ($|a_2|$) and FAD ($|a_1|$) versus the intracellular pO_2. These data were collected for A549 (blue circles), HeLa (green triangles) and HepG2 (red rectangles) cells; empty black circles show the results for A549 cells treated with rotenone/antimycin and empty black squares show the results for HepG2 cells treated with DNP. The error bars are the standard errors of the mean from at least 30 cells. (For interpretation of the references to color in this figure legend, the reader is referred to the Web version of this article.)

bound FAD ($|a_1|$) were obtained for A549 cells as compared to the other cell types, whereas HepG2 cells had the highest free NAD(P)H and lowest free and bound FAD.

The results shown in Figs. 1 and 2, led us to characterize A549 cells to have lower glycolysis and more active mitochondria capable of higher O_2 consumption as compared to the other cell types. HepG2 cells, in contrast, exhibited higher glycolytic activity and lower O_2 consumption. The effect of O_2 consumption on free and bound NAD(P)H and FAD production was further studied by disrupting O_2 consumption in A549 cells with rotenone/antimycin and enhancing O_2 consumption in HepG2 cells with DNP (see Supplemental Fig. S1 for the effects of inhibitors and uncoupler on the operations of ETC). As shown in Fig. 2, higher anaerobic glycolysis under a rotenone/antimycin treated condition was accompanied by higher free NAD(P)H and lower free and bound FAD production in A549 cells. Free NAD(P)H production decreased, and free and bound FAD productions increased in HepG2 cells treated with DNP. Bound NAD(P)H decreased by 1.8% upon rotenone/antimycin treatment and did not show any significant changes upon DNP treatment. Mann-Whitney tests showed a statistically significant difference between the concentrations of free NAD(P)H, free FAD and bound FAD in both types of cells in all possible pairwise combinations; the maximum p-value of the considered differences was ≤ 0.018. Except for A549 cells and those treated with rotenone/antimycin (p-value = 0.001), the differences between the concentration of bound NAD(P)H were not statistically significant among the cells.

Intracellular pseudocolor mapping of Myo-mCherry lifetime, pO_2 and the corresponding free/bound NAD(P)H ratio (a_1%/a_2%) in an exemplary A549, HeLa, and HepG2 cell at imposed pO_2 = 30–40 mmHg (O_2 = 4%) are shown in Fig. 3A, B and C, respectively. The values of 30–40 mmHg are equivalent to physiological pO_2 levels in tissue [27,43]. The color heat-map in Fig. 3B is based on the measurement of Myo-mCherry lifetime shown in Fig. 3A. Comparing Fig. 3B and C, it is possible to see how the higher free/bound NAD(P)H values (bluer values in panel C) tend to co-localize with regions of lower pO_2 (redder values in panel B) within the cells.

3.3. *Imaging of the metabolic state of the cells in response to intracellular pO_2*

Both FLIRR and ORR reflect the joint effects of OXPHOS and glycolysis on cellular metabolism and O_2 consumption [18,44]. In the commonly used intensity-based ORR, increased metabolic activity is denoted by an increase in the FAD/(FAD + NAD(P)H) ratio due to the conversion of fluorescent NAD(P)H to non-fluorescent NAD^+, and conversion of non-fluorescent $FADH_2$ to fluorescent FAD [1,12,19]. FLIRR ($a_{2,NAD(P)H}$ %/$a_{1,FAD}$ %) also increases with increased metabolic activity, meeting the same objective as a redox parameter [10]. Here, we pooled the intracellular pO_2 data corresponding to each imposed external pO_2 (acquired from Myo-mCherry FLIM shown in Fig. 1B) and correlated them with FLIRR and ORR to monitor the metabolic shift from OXPHOS to glycolysis. A sigmoidal behavior was observed when

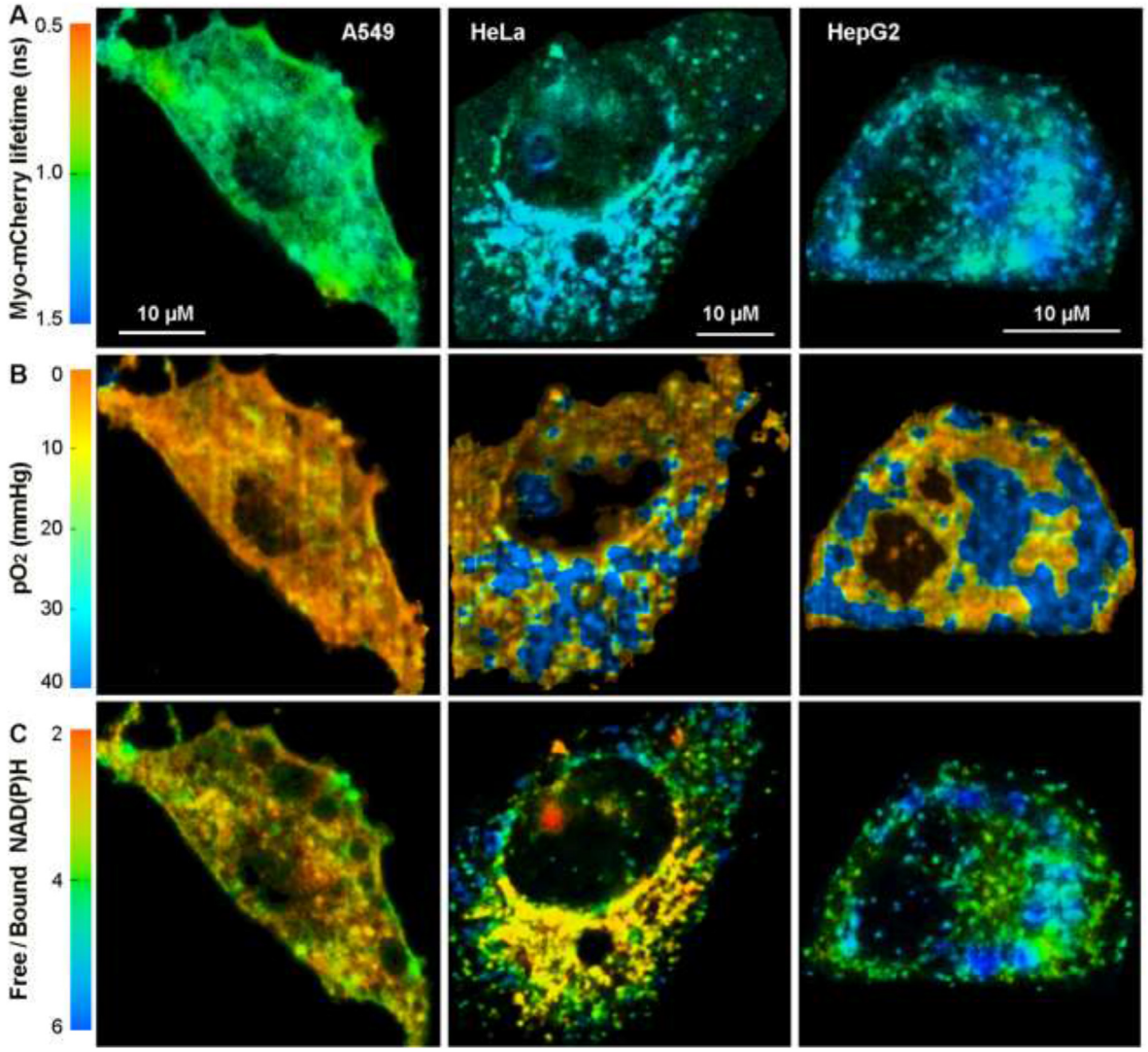

Fig. 3. Simultaneous mapping of the intracellular pO_2 and corresponding free/bound NAD(P)H. Pseudocolor mapping of A) Myo-mCherry fluorescence lifetime, B) apparent intracellular pO_2, and C) corresponding free and enzyme-bound NAD(P)H ratio ($a_1\%/a_2\%$) in the intracellular environment of A549, HeLa and HepG2 cells in response to imposed physiological pO_2 = 30–40 mmHg. Intracellular pO_2 distribution was obtained from the Myo-mCherry lifetime images and rotenone/antimycin calibration curve. In the color bars, red indicates lower values, whereas blue indicates higher values (of either lifetime, pO_2 or $a_1\%/a_2\%$). (For interpretation of the references to color in this figure legend, the reader is referred to the Web version of this article.)

plotting FLIRR (see Fig. 4A) and ORR (see Fig. 4B) versus the intracellular pO_2 in A549, HeLa, and HepG2 cells. Elevated FLIRR and ORR values seem correlated with higher intracellular O_2 consumption (lower pO_2). A549 cells with higher mitochondrial O_2 consumption (confirmed by rotenone/antimycin measurement in Fig. 1) showed the highest FLIRR and ORR values among the cells, whereas HepG2 cells with the lowest O_2 consumption had the lowest redox ratio. However, the differences between the redox ratios among the cells were not the same for ORR and FLIRR. This is because FLIRR measurement is unaffected by intensity-based limitations such as light scattering, absorption and the need for varying laser power levels to acquire sufficient photons (especially for FAD, with much lower concentration compared to NADH) [10,14]. Based on both ORR and FLIRR results, we expect that the relative contribution of OXPHOS to cellular energy production in A549 cells is higher than those obtained for HeLa and HepG2 cells. A decrease of FLIRR and ORR at intracellular $pO_2 \leq 10$ mmHg in A549 cells, $pO_2 \leq 17$ mmHg in HeLa cells and $pO_2 \leq 28$ mmHg in HepG2 cells implies a metabolic shift from OXPHOS toward glycolysis in these cells [10,19]. Fig. 4 also shows the metabolic response of A549 cells to the mitochondrial inhibitors and HepG2 cells to the mitochondrial uncoupler. FLIRR, ORR and O_2 consumption in A549 cells dropped to their lowest levels after shutting down OXPHOS with rotenone/antimycin. FLIRR decreased by 10% to 0.208 ± 0.014 at the highest pO_2 level and by 32% to 0.197 ± 0.026 at hypoxia. ORR dropped by 28–30% to (0.118–0.115) ± 0.018 at all imposed pO_2. The addition of DNP to HepG2 cells resulted in the substantial increase of FLIRR, ORR, and O_2 consumption due to the limited reduction of NAD^+ to NAD(P)H (see Fig. 2). FLIRR increased by 34% to 0.396 ± 0.023 at the highest pO_2 and by 23% to 0.316 ± 0.040 at hypoxia. ORR increased by 20–21% to 0.169 ± 0.030 at the highest pO_2 and to 0.158 ± 0.025 at hypoxia. The overall statistical analyses of FLIRR and ORR differences among the cells shows that these parameters are significantly different among the cell lines, with the exception of the pair untreated A549 cells–DNP-treated HepG2 cells. Mann-Whitney tests showed p-value = 0.96 for A549 cells and the DNP-treated HepG2 cells and p-values ≤ 0.01 for all other possible pairwise combinations. Intracellular pseudocolor mapping of FLIRR and ORR exemplary of A549, HeLa, and HepG2 cells are shown in Fig. 4C and D at physiological pO_2 (imposed pO_2 = 30–40 mmHg); the red and blue colors show the smallest and

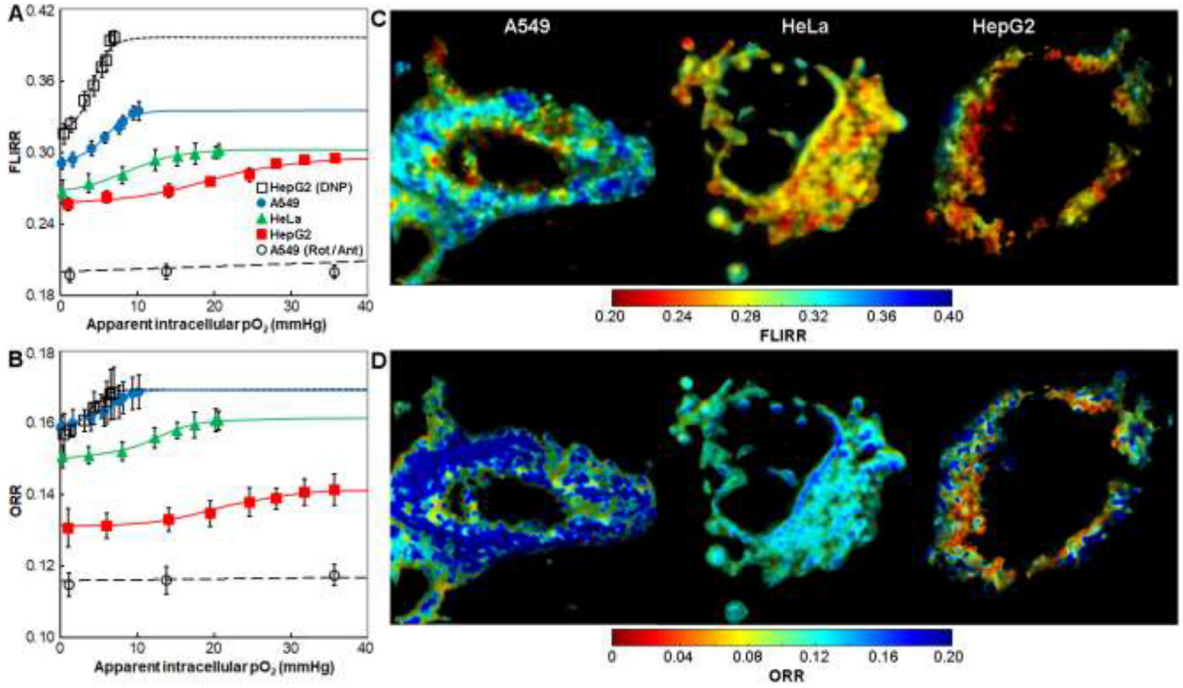

Fig. 4. The effects of pO_2 on fluorescence lifetime redox ratio (FLIRR) and optical redox ratio (ORR). A-B) The changes of FLIRR and ORR in response to the intracellular pO_2 in A549 (blue circle), HeLa (green triangle), and HepG2 (red square) cells demonstrate that the more active cells are more oxidative and retain OXPHOS further into anoxia. A549 cells treated with rotenone/antimycin and HepG2 cells treated with DNP are shown with empty black circles and empty black squares, respectively. The error bars are the standard error of the mean from at least 30 cells. C-D) Pseudocolor mapping of FLIRR and ORR in the intracellular environment of A549, HeLa, and HepG2 cells in response to imposed physiological pO_2 = 30–40 mmHg; red and blue indicate smaller and larger FLIRR or ORR, respectively. (For interpretation of the references to color in this figure legend, the reader is referred to the Web version of this article.)

largest redox ratio, respectively.

The redirection of energy metabolism from OXPHOS to glycolysis is largely orchestrated by protein interactions that are involved in programming the core hallmarks of cancer. Growing evidence indicates that tumor suppressors and oncogenes reprogram glucose metabolism and impact tumor phenotypes via Pyruvate kinase M2 (PKM2) [32,45]. The interaction of Small Ubiquitin-like Modifier-E3 (SUMO-E3) ligase with PKM2 promotes PKM2 entering the nucleus and enhances Warburg effects. In contrast, heat shock protein 40 kD (HSP40) interacts with PKM2 to degrade it, and shunts glycolysis into OXPHOS. It is also reported that HSP40 knockdown reduces O_2 consumption. Detailed studies of PKM2-HSP40 interactions, glucose consumption and lactate production in A549, HeLa and HepG2 cells can be found elsewhere [32].

4. Conclusions

Historically, oxygenation and metabolic imaging in live cells have been explored individually under ambient atmosphere (O_2 = 21%). Mammalian cells, however, are generally adapted to interstitial O_2 levels much lower than atmospheric conditions [29,30] and to our knowledge no previous work has been presented where metabolic changes are tracked at imposed near-physiological pO_2 levels simultaneously with measurements of the apparent intracellular pO_2. The goal of this study was to image and quantify the correlation between intracellular pO_2 and metabolism in A549, HeLa and HepG2 cells under various media-imposed pO_2 levels ranging from normoxia to hypoxia. We presented here a non-invasive, straightforward, and quantitative method for imaging intracellular pO_2 and the corresponding NAD(P)H and FAD partition into free and bound pools at different imposed pO_2. As is the case in other highly proliferative cells [5], the ratio of free/bound NAD(P)H ($3 \leq a_1\%/a_2\%$) was high in A549, HeLa, and HepG2 cells at all imposed pO_2 levels. However, our measurements revealed pO_2, NAD(P)H, and FAD heterogeneity both at the intra- and intercellular level, as well as among different cell types. The O_2 consumption and OXPHOS contribution to cellular energy production was the highest in A549 cells; whereas HepG2 cells showed the lowest level of O_2 consumption and the highest glycolytic rate as compared to the other cell types. The relationship between intracellular pO_2 and metabolic redox ratio, FLIRR or ORR, calculated from NAD(P)H and FAD was best described by a sigmoid-shaped curve, and from these data it is possible to infer a metabolic shift from OXPHOS toward glycolysis at lower pO_2 for all cell types studied here with a trend for retention of more OXPHOS character at lower pO_2 by the more active cell types.

Being able to simultaneously image intracellular pO_2 and metabolism is a paramount objective, as it could allow physiological and pathological metabolic processes to be tracked in dynamic systems. It also enhances our ability to precisely quantify the role of intracellular O_2 consumption in cellular energy production and metabolism *in vitro* and *in vivo*. Multiphoton redox and pO_2 imaging also have broad applicability in the study of diseases outside of cancer where metabolism is altered, such as Alzheimer's disease, diabetes, coronary heart disease, and others, as well as studying metabolism in development and aging. The great advantage of the multiphoton FLIM probes and strategies demonstrated here is their direct applicability to such systems *in vivo*, in a minimally invasive fashion, while delivering quantitative and accurate information.

Author contribution

R.P.; Designed and performed experiments, analyzed most of the data and wrote the paper. B.R., and A.G.; Performed FLIM, part of the data analyses and western blotting. G.A.; Performed confocal imaging and analyses of mitochondrial volume, and generated pseudocolor mapping of pO_2, FLIRR and ORR. A.A.; Prepared the plasmid and calibrated the FLIM setup. A.P.; Examined the Myo-mCherry transfection efficiency and cytotoxicity. D.L.S. and J.R.K.; Supervised the research.

Declaration of competing interest

The authors declare no competing interests.

Acknowledgements

This work was supported by the Intramural Research Program of the National Heart, Lung, and Blood Institute (NHLBI), and in part by Intramural Training and Education (OITE) and the Intramural Research Program of the Eunice Kennedy Shriver National Institute of Child Health and Human Development (NICHD), National Institutes of Health (NIH). We would like to acknowledge the Light Microscopy Core at NHLBI for the use of their confocal microscopes for fluorescence lifetime imaging. We thank Dr. Evelyn Ralston and Aster Kenea from Light Imaging Section at National Institute of Arthritis and Musculoskeletal and Skin Diseases (NIAMS) for assistance with Incucyte imaging. We also thank Dr. Christian A. Combs, Director of NHLBI Light Microscopy Core and Dr. Jay H. Chung from Laboratory of Obesity and Aging Research at NHLBI for helpful discussion.

Appendix A. Supplementary data

Supplementary data to this article can be found online at https://doi.org/10.1016/j.redox.2020.101549.

References

[1] C. Stringari, L. Abdeladim, G. Malkinson, P. Mahou, X. Solinas, I. Lamarre, et al., Multicolor two-photon imaging of endogenous fluorophores in living tissues by wavelength mixing, Sci. Rep. 7 (2017) 3792, https://doi.org/10.1038/s41598-017-03359-8.

[2] H.D. Vishwasrao, A.A. Heikal, K.A. Kasischke, W.W. Webb, Conformational dependence of intracellular NADH on metabolic state revealed by associated fluorescence anisotropy, J. Biol. Chem. 280 (2005) 25119–25126, https://doi.org/10.1074/jbc.M502475200 PubMed PMID: 15863500.

[3] V.V. Ghukasyan, F.-J. Kao, Monitoring cellular metabolism with fluorescence lifetime of reduced nicotinamide adenine dinucleotide, J. Phys. Chem. C 113 (2009) 11532–11540, https://doi.org/10.1021/jp810931u.

[4] G. Yellen, Fueling thought: management of glycolysis and oxidative phosphorylation in neuronal metabolism, J. Cell Biol. 217 (2018) 2235–2246, https://doi.org/10.1083/jcb.201803152 PubMed PMID: 29752396; PubMed Central PMCID: PMC6028533.

[5] C. Stringari, R.A. Edwards, K.T. Pate, M.L. Waterman, P.J. Donovan, E. Gratton, Metabolic trajectory of cellular differentiation in small intestine by Phasor Fluorescence Lifetime Microscopy of NADH, Sci. Rep. 2 (2012) 568, https://doi.org/10.1038/srep00568 Epub 2012/08/15, PubMed PMID: 22891156; PubMed Central PMCID: PMCPMC3416911.

[6] T.A. Giancaspero, G. Busco, C. Panebianco, C. Carmone, A. Miccolis, G.M. Liuzzi, et al., FAD synthesis and degradation in the nucleus create a local flavin cofactor pool, J. Biol. Chem. 288 (2013) 29069–29080, https://doi.org/10.1074/jbc.M113.500066 Epub 2013/08/16, PubMed PMID: 23946482; PubMed Central PMCID: PMCPMC3790006.

[7] M. Barile, T.A. Giancaspero, C. Brizio, C. Panebianco, C. Indiveri, M. Galluccio, et al., Biosynthesis of flavin cofactors in man: implications in health and disease, Curr. Pharmaceut. Des. 19 (2013) 2649–2675 PubMed PMID: 23116402 , Accessed date: 3 November 2012.

[8] Y. Zhang, A.-W. Mohsen, C. Kochersperger, K. Solo, A.V. Schmidt, J. Vockley, et al., An acyl-CoA dehydrogenase microplate activity assay using recombinant porcine electron transfer flavoprotein, Anal. Biochem. 581 (2019) 113332, https://doi.org/10.1016/j.ab.2019.06.003.

[9] Z. Swigonová, A.-W. Mohsen, J. Vockley, Acyl-CoA dehydrogenases: dynamic history of protein family evolution, J. Mol. Evol. 69 (2009) 176–193, https://doi.org/10.1007/s00239-009-9263-0 Epub 2009/07/29, PubMed PMID: 19639238.

[10] H. Wallrabe, Z. Svindrych, S.R. Alam, K.H. Siller, T. Wang, D. Kashatus, et al., Segmented cell analyses to measure redox states of autofluorescent NAD(P)H, FAD & Trp in cancer cells by FLIM, Sci. Rep. 8 (2018) 79, https://doi.org/10.1038/s41598-017-18634-x Epub 2018/01/10, PubMed PMID: 29311591; PubMed Central PMCID: PMCPMC5758727.

[11] F. Bartolome, A.Y. Abramov, Measurement of mitochondrial NADH and FAD autofluorescence in live cells, Methods Mol. Biol. 1264 (2015) 263–270, https://doi.org/10.1007/978-1-4939-2257-4_23 PubMed PMID: 25631020.

[12] M.C. Skala, K.M. Riching, A. Gendron-Fitzpatrick, J. Eickhoff, K.W. Eliceiri, J.G. White, et al., In vivo multiphoton microscopy of NADH and FAD redox states, fluorescence lifetimes, and cellular morphology in precancerous epithelia, Proc. Natl. Acad. Sci. U.S.A. 104 (2007) 19494–19499, https://doi.org/10.1073/pnas.0708425104 PubMed PMID: 18042710; PubMed Central PMCID: PMCPMC2148317.

[13] T.S. Blacker, M.R. Duchen, Investigating mitochondrial redox state using NADH and NADPH autofluorescence, Free Radic. Biol. Med. 100 (2016) 53–65, https://doi.org/10.1016/j.freeradbiomed.2016.08.010 Epub 2016/08/09, PubMed PMID: 27519271.

[14] R. Cao, H. Wallrabe, K. Siller, S. Rehman Alam, A. Periasamy, Single-cell redox states analyzed by fluorescence lifetime metrics and tryptophan FRET interaction with NAD(P)H, Cytometry 95 (2019) 110–121, https://doi.org/10.1002/cyto.a.23711.

[15] J.H. Ostrander, C.M. McMahon, S. Lem, S.R. Millon, J.Q. Brown, V.L. Seewaldt, et al., Optical redox ratio differentiates breast cancer cell lines based on estrogen receptor status, Canc. Res. 70 (2010) 4759–4766, https://doi.org/10.1158/0008-5472.CAN-09-2572 Epub 2010/05/13, PubMed PMID: 20460512; PubMed Central PMCID: PMCPMC3826951.

[16] A.V. Zhdanov, V.I. Ogurtsov, C.T. Taylor, D.B. Papkovsky, Monitoring of cell oxygenation and responses to metabolic stimulation by intracellular oxygen sensing technique, Integrative Biology 2 (2010) 443–451, https://doi.org/10.1039/C0IB00021C.

[17] L.A. Pham-Huy, H. He, C. Pham-Huy, Free radicals, antioxidants in disease and health, Int. J. Biomed. Sci. 4 (2008) 89–96 PubMed PMID: 23675073; PubMed Central PMCID: PMCPMC3614697.

[18] K.P. Quinn, G.V. Sridharan, R.S. Hayden, D.L. Kaplan, K. Lee, I. Georgakoudi, Quantitative metabolic imaging using endogenous fluorescence to detect stem cell differentiation, Sci. Rep. 3 (2013) 3432, https://doi.org/10.1038/srep03432 PubMed PMID: 24305550; PubMed Central PMCID: PMC3851884.

[19] J. Hou, H.J. Wright, N. Chan, R. Tran, O.V. Razorenova, E.O. Potma, et al., Correlating two-photon excited fluorescence imaging of breast cancer cellular redox state with seahorse flux analysis of normalized cellular oxygen consumption, J. Biomed. Optic. 21 (2016) 60503, https://doi.org/10.1117/1.JBO.21.6.060503 PubMed PMID: 27300321; PubMed Central PMCID: PMC4906146.

[20] H. Wallrabe, Z. Svindrych, S.R. Alam, K.H. Siller, T. Wang, D. Kashatus, et al., Segmented cell analyses to measure redox states of autofluorescent NAD(P)H, FAD & Trp in cancer cells by FLIM, Sci. Rep. 8 (2018) 79, https://doi.org/10.1038/s41598-017-18634-x Epub 2018/01/10, PubMed PMID: 29311591; PubMed Central PMCID: PMCPMC5758727.

[21] D.M. Jameson, V. Thomas, D.M. Zhou, Time-resolved fluorescence studies on NADH bound to mitochondrial malate dehydrogenase, Biochim. Biophys. Acta 994 (1989) 187–190, https://doi.org/10.1016/0167-4838(89)90159-3 PubMed PMID: 2910350.

[22] K. Blinova, S. Carroll, S. Bose, A.V. Smirnov, J.J. Harvey, J.R. Knutson, et al., Distribution of mitochondrial NADH fluorescence lifetimes: steady-state kinetics of matrix NADH interactions, Biochemistry 44 (2005) 2585–2594, https://doi.org/10.1021/bi0485124 PubMed PMID: 15709771.

[23] J.H. Ostrander, C.M. McMahon, S. Lem, S.R. Millon, J.Q. Brown, V.L. Seewaldt, et al., Optical redox ratio differentiates breast cancer cell lines based on estrogen receptor status, Canc. Res. 70 (2010) 4759–4766, https://doi.org/10.1158/0008-5472.CAN-09-2572 Epub 2010/05/13, PubMed PMID: 20460512; PubMed Central PMCID: PMCPMC3826951.

[24] R. Penjweini, A. Andreoni, T. Rosales, J. Kim, M.D. Brenner, D.L. Sackett, et al., Intracellular oxygen mapping using a myoglobin-mCherry probe with fluorescence lifetime imaging, J. Biomed. Optic. 23 (2018) 1–14, https://doi.org/10.1117/1.JBO.23.10.107001 PubMed PMID: 30298706; PubMed Central PMCID: PMC6210794.

[25] V. Vargas, J.E. Brunet, D.M. Jameson, Oxygen diffusion near the heme binding site of horseradish peroxidase, Biochem. Biophys. Res. Commun. 178 (1991) 104–109, https://doi.org/10.1016/0006-291x(91)91785-b PubMed PMID: 2069551.

[26] S. Sandeep Sharma, D. Deepa Rawat, Partial Pressure of Oxygen (PO2), Treasure Island (FL), StatPearls Publishing, 2019.

[27] S. Subramani, P. Kanthakumar, D. Maneksh, A. Sidharthan, S.V. Rao, V. Parasuraman, et al., O2-CO2 diagram as a tool for comprehension of blood gas abnormalities, Adv. Physiol. Educ. 35 (2011) 314–320, https://doi.org/10.1152/advan.00110.2010 PubMed PMID: 21908843.

[28] E.G. Mik, T. Johannes, C.J. Zuurbier, A. Heinen, J.H. Houben-Weerts, G.M. Balestra, et al., In vivo mitochondrial oxygen tension measured by a delayed fluorescence lifetime technique, Biophys. J. 95 (2008) 3977–3990, https://doi.org/10.1529/biophysj.107.126094 PubMed PMID: 18641065; PubMed Central PMCID: PMC2553111.

[29] M. Yazdani, Technical aspects of oxygen level regulation in primary cell cultures: a review, Interdiscip, Toxicol 9 (2016) 85–89, https://doi.org/10.1515/intox-2016-0011 PubMed PMID: 28652851; PubMed Central PMCID: PMC5464680.

[30] A. Al-Ani, D. Toms, D. Kondro, J. Thundathil, Y. Yu, M. Ungrin, Oxygenation in cell culture: critical parameters for reproducibility are routinely not reported, PloS One 13 (2018) e0204269, , https://doi.org/10.1371/journal.pone.0204269 PubMed PMID: 30325922; PubMed Central PMCID: PMC6191109.

[31] N.A. Rahim, S. Pelet, R.D. Kamm, P.T. So, Methodological considerations for global analysis of cellular FLIM/FRET measurements, J. Biomed. Optic. 17 (2012) 026013, , https://doi.org/10.1117/1.JBO.17.2.026013 PubMed PMID: 22463045; PubMed Central PMCID: PMC3382354.

[32] L. Huang, Z. Yu, T. Zhang, X. Zhao, G. Huang, HSP40 interacts with pyruvate kinase M2 and regulates glycolysis and cell proliferation in tumor cells, PloS One 9 (2014) e92949, , https://doi.org/10.1371/journal.pone.0092949 PubMed PMID: 24658033; PubMed Central PMCID: PMCPMC3962495.

[33] D. Loiseau, A. Chevrollier, O. Douay, F. Vavasseur, G. Renier, P. Reynier, et al., Oxygen consumption and expression of the adenine nucleotide translocator in cells lacking mitochondrial DNA, Exp. Cell Res. 278 (2002) 12–18, https://doi.org/10.1006/excr.2002.5553 PubMed PMID: 12126953.

[34] A. Andreoni, R. Penjweini, B. Roarke, M.-P. Strub, D.L. Sackett, J.R. Knutson,

Genetically encoded FRET probes for direct mapping and quantification of intracellular oxygenation level via fluorescence lifetime imaging, SAVE Proc. (2019) 108820O, https://doi.org/10.1117/12.2510646 SPIE 10882.
[35] X. Chen, J.L. Zaro, W.C. Shen, Fusion protein linkers: property, design and functionality, Adv. Drug Deliv. Rev. 65 (2013) 1357–1369, https://doi.org/10.1016/j.addr.2012.09.039 PubMed PMID: 23026637; PubMed Central PMCID: PMC3726540.
[36] A.S. Golub, R.N. Pittman, Oxygen dependence of respiration in rat spinotrapezius muscle in situ, Am. J. Physiol. Heart Circ. Physiol. 303 (2012) H47–H56, https://doi.org/10.1152/ajpheart.00131.2012 PubMed PMID: 22523254; PubMed Central PMCID: PMC3404650.
[37] R. Araki, M. Tamura, I. Yamazaki, The effect of intracellular oxygen concentration on lactate release, pyridine nucleotide reduction, and respiration rate in the rat cardiac tissue, Circ. Res. 53 (1983) 448–455 PubMed PMID: 6627604.
[38] T.P. Keeley, G.E. Mann, Defining physiological normoxia for improved translation of cell physiology to animal models and humans, Physiol. Rev. 99 (2019) 161–234, https://doi.org/10.1152/physrev.00041.2017 PubMed PMID: 30354965.
[39] V.V. Ghukasyan, F.-J. Kao, Monitoring cellular metabolism with fluorescence lifetime of reduced nicotinamide adenine dinucleotide, J. Phys. Chem. C 113 (2009) 11532–11540, https://doi.org/10.1021/jp810931u.
[40] M.A. Yaseen, S. Sakadzic, W. Wu, W. Becker, K.A. Kasischke, D.A. Boas, In vivo imaging of cerebral energy metabolism with two-photon fluorescence lifetime microscopy of NADH, Biomed. Optic Express 4 (2013) 307–321, https://doi.org/10.1364/BOE.4.000307 PubMed PMID: 23412419; PubMed Central PMCID: PMC3567717.
[41] T.S. Blacker, Z.F. Mann, J.E. Gale, M. Ziegler, A.J. Bain, G. Szabadkai, et al., Separating NADH and NADPH fluorescence in live cells and tissues using FLIM, Nat. Commun. 5 (2014) 3936, https://doi.org/10.1038/ncomms4936 Epub 2014/05/31, PubMed PMID: 24874098; PubMed Central PMCID: PMCPMC4046109.
[42] M.A. Yaseen, J. Sutin, W. Wu, B. Fu, H. Uhlirova, A. Devor, et al., Fluorescence lifetime microscopy of NADH distinguishes alterations in cerebral metabolism in vivo, Biomed. Optic Express 8 (2017) 2368–2385, https://doi.org/10.1364/BOE.8.002368 Epub 2017/07/01, PubMed PMID: 28663879; PubMed Central PMCID: PMCPMC5480486.
[43] T.C. Zhu, B. Liu, R. Penjweini, Study of tissue oxygen supply rate in a macroscopic photodynamic therapy singlet oxygen model, J. Biomed. Optic. 20 (2015) 38001, https://doi.org/10.1117/1.JBO.20.3.038001 PubMed PMID: 25741665.
[44] J. Hou, H.J. Wright, N. Chan, R. Tran, O.V. Razorenova, E.O. Potma, et al., Correlating two-photon excited fluorescence imaging of breast cancer cellular redox state with seahorse flux analysis of normalized cellular oxygen consumption, J. Biomed. Optic. 21 (2016) 60503, https://doi.org/10.1117/1.JBO.21.6.060503 PubMed PMID: 27300321; PubMed Central PMCID: PMC4906146.
[45] H. Le, Dual roles of PKM2 in cancer metabolism, Acta biochimica et. biophysica Sinica. 45 (2012), https://doi.org/10.1093/abbs/gms106.